

Ultrahigh Thermoelectric Performance in $\text{SrNb}_{0.2}\text{Ti}_{0.8}\text{O}_3$ Oxide Films at a Submicrometer-Scale Thickness

Jikun Chen,^{*,†,‡,§,○,¶,□} Hongyi Chen,^{‡,○} Feng Hao,[‡] Xinyou Ke,^{||} Nuofu Chen,^{⊥,□} Takeaki Yajima,[§] Yong Jiang,[†] Xun Shi,[‡] Kexiong Zhou,[‡] Max Döbeli,[#] Tiansong Zhang,[‡] Binghui Ge,[▽] Hongliang Dong,[◆] Huarong Zeng,[‡] Wenwang Wu,[¶] and Lidong Chen,^{*,‡}

[†]School of Materials Science and Engineering, University of Science and Technology Beijing, Beijing 100083, China

[‡]Shanghai Institute of Ceramics, Chinese Academy of Sciences, Shanghai 200050, China

[§]School of Engineering, The University of Tokyo, Tokyo 1138656, Japan

^{||}John A. Paulson School of Engineering and Applied Sciences, Harvard University, Cambridge, Massachusetts 02138, United States

[⊥]School of Renewable Energy, North China Electric Power University, Beijing 102206, China

[#]Ion Beam Physics, ETH Zurich, CH-8093 Zurich, Switzerland

[▽]Beijing National Laboratory for Condensed Matter Physics, Chinese Academy of Sciences, Beijing 100190, China

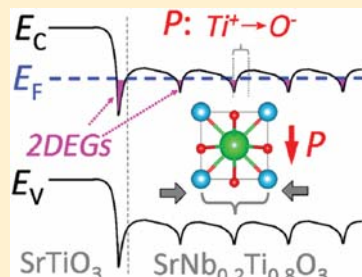
[◆]Center for High Pressure Science and Technology Advanced Research, Shanghai 201203, China

[¶]Institute of Advanced Structure Technology, Beijing Institute of Technology, Beijing 100081, China

HPSTAR
487-2018

Supporting Information

ABSTRACT: Localized refrigeration and power generation via thermoelectric technology rely on efficient thermoelectric materials with high performance at room temperature. Although the two-dimensional electron gas (2DEG)-related materials exhibit ultrahigh thermoelectric performance near room temperature, such performance is only preserved at thicknesses within subnanometer scales, limited by the requirement of two-dimensional size confinements. Here we report ultrahigh thermoelectric performance similar to 2DEG-related materials but achieved in $\text{SrNb}_{0.2}\text{Ti}_{0.8}\text{O}_3$ oxide films with a submicrometer-scale thickness by regulating strain-induced lattice polarizations and interfacial polarizations. A large figure of merit, zT , and power factor ($\sim 10^2\text{--}10^3 \mu\text{W cm}^{-1}\text{K}^{-2}$) were achieved near room temperature, and the maximum zT is estimated to be ~ 1.6 for a 49 nm thick film. These performances exceed those of the existing n-type thermoelectric materials for room-temperature uses and the reported best oxide materials beyond subnanometer scales. The earth-abundant elemental composition of the oxide film paves the way toward potential applications in thermoelectric thin film devices with a microscale thickness.



Thermoelectric (TE) materials achieve localized conversion between thermal and electric energies, and the conversion efficiency is determined by a figure of merit $zT = S^2\sigma T\kappa^{-1}$, where S is the Seebeck coefficient, σ the electrical conductivity, T the absolute temperature, and κ the thermal conductivity.^{1–16} Efforts to raise the zT value have been focused on two aspects: reducing the lattice thermal conductivity (κ_{lattice})^{10,11} and improving power factors (PF = $S^2\sigma$).^{12,13} Since the 1990s, the κ_{lattice} for many TE material systems has been reduced near the amorphous limit by using phonon scattering approaches, such as fabricating nanostructures,¹⁰ point defects,¹¹ and rattling filler ions within cage structures.¹² Therefore, it draws more potential to optimize the electronic component: PF = $S^2\sigma$.¹³ To date, two-dimensional electron gas (2DEG)-related TE materials hold the record for

zT and PF near room temperature.^{1–5} The generation of 2DEGs is driven by spatial confinement along the direction of thickness by making superlattice (or quantum dot) structured $\text{Bi}_2\text{Te}_3/\text{Sb}_2\text{Te}_3$,¹ PbSeTe ,² or $\text{SrNb}_{0.2}\text{Ti}_{0.8}\text{O}_3/\text{SrTiO}_3$ ^{3–5} or is observed at the interface of $\text{TiO}_2/\text{SrTiO}_3$ ³ and $\text{LaAlO}_3/\text{SrTiO}_3$.^{7,8} When the thickness of these TE materials is spatially confined within a subnanometer scale, the two-dimensional confinement of carriers enlarges the density of states near the Fermi energy^{3–6} and triggers electron phonon coupling (EPC).^{7–9} This overcomes the conventional σ - S trade-off to more independently improves S and thereby further increases

Received: March 4, 2017

Accepted: March 24, 2017

Published: March 24, 2017

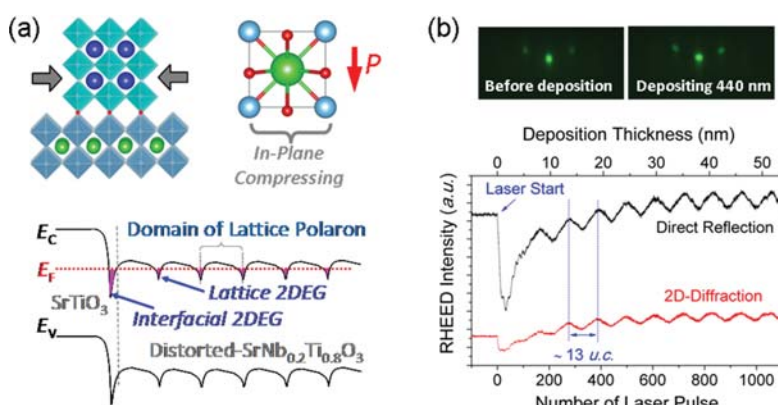


Figure 1. (a) Schematic illustrations of compressive interfacial strain-induced lattice polarization and the periodic coulomb regulation of the band structure. (b) RHEED patterns and intensity oscillations for the present deposition of $\text{SrNb}_{0.2}\text{Ti}_{0.8}\text{O}_3$ on a $\text{SrTiO}_3(001)$ substrate.

PF.⁶ Nevertheless, the preserved large S at a high carrier concentration (n) in 2DEG-related materials is strongly dependent on two-dimensional (2D) spatial confinement of carriers.^{1–5} As observed for the $\text{SrNb}_{0.2}\text{Ti}_{0.8}\text{O}_3/\text{SrTiO}_3$ superlattice, the Seebeck coefficient is reduced sharply when the thickness of $\text{SrNb}_{0.2}\text{Ti}_{0.8}\text{O}_3$ exceeds three unit cells (~1.2 nm).^{3–5} The prerequisite of spatial confinement largely impedes practical applications of the present 2DEG materials for high power energy conversions as the amount of TE material is insufficient. How to break through the limitation of the size confinement and increase the effective thickness past a nanometer scale are critical issues to address.

Using the polarizations and polar discontinuity in materials with asymmetric charge centers provides an alternative direction to regulate 2DEGs that does not strongly rely on spatial confinement.^{17–21} As typical examples reported for wurtzite AlGaN/GaN heterostructures, the direction of spontaneous lattice polarization was ordered by binding with the interfacial polarization charge using appropriate epitaxy strategies.¹⁷ The polarization- and polar discontinuity-induced internal electrostatic field significantly influences the distribution, density, and mobility of 2DEGs.^{17,18,20,21} Similarly, polarization-associated planar charge localizations within $\text{LaAlO}_3/\text{SrTiO}_3$ and $\text{La}_{0.5}\text{Sr}_{0.5}\text{TiO}_3/\text{SrTiO}_3$ interfaces were also recognized as important factors to achieve electronic confinement of 2D carriers to form 2DEGs.^{7–9} The observed phonon drag enhancement in S was reported as a benchmark of EPC between the carriers and interfacial polarons within $\text{LaAlO}_3/\text{SrTiO}_3$.^{7,8} Here, we report ultrahigh TE performance similar to those of 2DEG-related materials achieved in a micrometer thick $\text{SrNb}_{0.2}\text{Ti}_{0.8}\text{O}_3$ film by introducing both strain-induced lattice polarizations and interfacial polarizations. Compared with reported 2DEG-related $\text{SrNb}_{0.2}\text{Ti}_{0.8}\text{O}_3$, the film thickness to maintain a large Seebeck coefficient at high carrier concentration is effectively enhanced by three orders from a subnanometer scale to a micrometer scale. As-observed high performance is demonstrated to be an indication of the presence of lattice and interaction polarizations, and a possible mechanism is proposed.

To introduce both lattice and interfacial polarizations, the $\text{SrNb}_{0.2}\text{Ti}_{0.8}\text{O}_3$ films were coherently grown on a single-crystal $\text{SrTiO}_3(001)$ substrate by pulsed laser deposition (PLD). As illustrated by Figure 1a, the unit cell of co-lattice-grown $\text{SrNb}_{0.2}\text{Ti}_{0.8}\text{O}_3$ is compressively distorted by biaxial in-plane interfacial strain because it possesses a larger bulk lattice

constant ($a_0 = 3.96 \text{ \AA}$) than SrTiO_3 ($a_0 = 3.905 \text{ \AA}$) with a lattice mismatch of ~1.41%. This has been demonstrated previously to separate the charge center of TiO_6 octahedra^{22–25} and generate cross-plane $\text{Ti}^+ \rightarrow \text{O}^-$ lattice dipoles (or polarons).²² The presence of a coherent interface between electron-doped and intrinsic SrTiO_3 is known to result in interfacial polarization, as observed in $\text{La}_{0.5}\text{Sr}_{0.5}\text{TiO}_3/\text{SrTiO}_3$ heterostructures.⁹ Under appropriate deposition kinetics, the cross-plane lattice polarizations are thermodynamically favored by binding with the interfacial polarizations, as previously observed for AlGaN/GaN heterostructures.^{17,18,20} The resultant periodical coulomb potentials along the cross-plane direction are expected to zigzag the conduction band across the Fermi energy and generate potential wells to confine the carriers, as illustrated by Figure 1a.

Figure 1b shows typical reflection high-energy electron diffraction (RHEED) patterns and their intensity oscillations during the deposition process. The same RHEED patterns before and after depositing over 10^3 unit cells (~440 nm) are observed. No significant change of the in-plane lattice constant from the surface region is indicated. Both the electron reflection and the two-dimensional electron diffraction RHEED patterns exhibit an intensity oscillation period of ~13 unit cells. It reveals a layer-by-layer growth mode with long-range orders to deposit each molecular layer. As-grown films possess the same crystal structure and orientation compared with the substrate, as their X-ray diffraction patterns shown in Figure S1. The film composition was measured as $\text{SrNb}_{0.2}\text{Ti}_{0.8}\text{O}_{2.7}$ by Rutherford backscattering (RBS).

The high-angle annular dark-field (HAADF) images of the interfaces between as-grown thin films and the underlying substrates are shown in Figure 2a. For the $\text{SrNb}_{0.2}\text{Ti}_{0.8}\text{O}_3/\text{SrTiO}_3$ sample, co-lattice-matched lattice atoms from the film and substrate are seen at their interfacial regions, with no detectable diffusion of the Nb element observed (see Figure S5). Further demonstration of the coherent epitaxy is verified by the same in-plane vectors of the film and substrate diffraction patterns in reciprocal space mappings (RSMs), as shown in Figure 2c. Similar RSM patterns were observed for more $\text{SrNb}_{0.2}\text{Ti}_{0.8}\text{O}_3/\text{SrTiO}_3$ samples with different film thicknesses varied from 49 nm to $2.2 \mu\text{m}$, as shown in Figure S2. These results demonstrate that the lattice of the film was in-plane-locked by the substrate when further increasing the deposition thickness across a micrometer scale. Therefore, the compressive interfacial strain is effectively imposed upon the

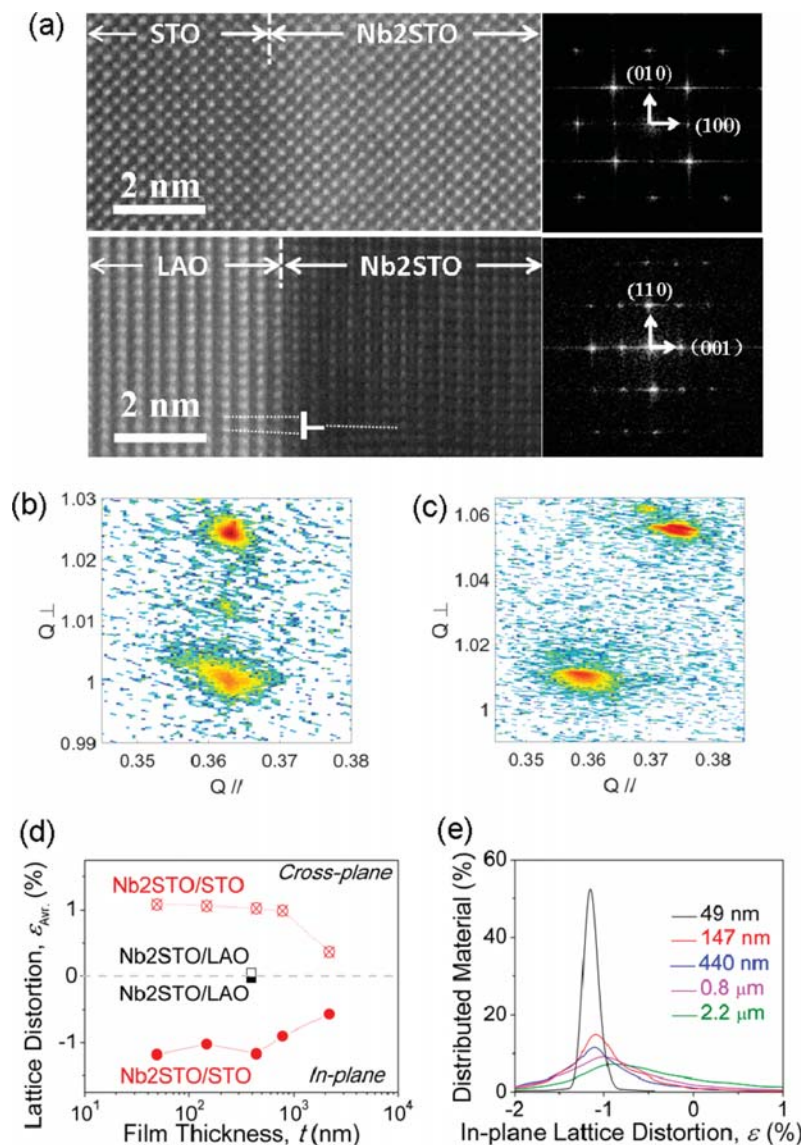


Figure 2. (a) HAADF images of the interfacial regions and Fourier transformation of the film materials for samples of $\text{SrNb}_{0.2}\text{Ti}_{0.8}\text{O}_3/\text{SrTiO}_3(001)$ and $\text{SrNb}_{0.2}\text{Ti}_{0.8}\text{O}_3/\text{LaAlO}_3(001)$. (b,c) Reciprocal space mapping (RSM) of $\text{SrNb}_{0.2}\text{Ti}_{0.8}\text{O}_3/\text{SrTiO}_3(001)$ samples with a film thickness of 440 nm (b) and $\text{SrNb}_{0.2}\text{Ti}_{0.8}\text{O}_3/\text{LaAlO}_3(001)$ samples with a film thickness of 393 nm (c). Q_{\parallel} and Q_{\perp} represent the in-plane and cross-plane reciprocal space vectors of [110] and [001], respectively. (d) Averaged in-plane and cross-plane lattice displacements ($\varepsilon_{\text{Avr.}}$) for $\text{SrNb}_{0.2}\text{Ti}_{0.8}\text{O}_3/\text{SrTiO}_3(001)$ samples with different film thicknesses, estimated from their RSM as shown in (b), (c), and Figure S2. (e) Proportion of material distributed at different values of $\varepsilon_{\parallel,\text{Avr.}}$ for $\text{SrNb}_{0.2}\text{Ti}_{0.8}\text{O}_3/\text{SrTiO}_3(001)$ at different deposition thicknesses estimated from the RSM results.

film materials. This is in contrast to the $\text{SrNb}_{0.2}\text{Ti}_{0.8}\text{O}_3/\text{LaAlO}_3$ sample deposited under the same conditions, in which case the interfacial strain relaxed fast owing to a larger lattice mismatch ($\sim 3.65\%$) between the film and substrate. The edge dislocations are clearly observed at the interfaces between the $\text{SrNb}_{0.2}\text{Ti}_{0.8}\text{O}_3$ films and the underlying LaAlO_3 substrates (see Figure 2a). From its RSM patterns shown by Figure 2c, the in-plane vectors are different for the films and substrates, indicating the relaxations of the interfacial strains.

On the basis of the RSM results, as shown in Figures 2b,c and S2, the averaged in-plane and cross-plane lattice displacements ($\varepsilon_{\parallel,\text{Avr.}}$ and $\varepsilon_{\perp,\text{Avr.}}$) are derived from the film pattern in the RSM by eq 1

$$\varepsilon_{\parallel(\perp),\text{Avr.}} = \frac{\int_{Q_{\parallel(\perp)}} \left[\left(\frac{(1/Q_{\parallel(\perp)}) - (1/Q_{\parallel(\perp)0})}{1/Q_{\parallel(\perp)0}} \right) \times \int_{Q_{\perp(\parallel)}} I_{\text{Film}}(Q_{\parallel}, Q_{\perp}) dQ_{\perp(\parallel)} \right] dQ_{\parallel(\perp)}}{\iint_{Q_{\parallel}Q_{\perp}} I_{\text{Film}}(Q_{\parallel}, Q_{\perp}) dQ_{\parallel} dQ_{\perp}} \quad (1)$$

where Q_{\parallel} and Q_{\perp} represent the in-plane and cross-plane reciprocal vectors, respectively and $I_{\text{Film}}(Q_{\parallel}, Q_{\perp})$ is the diffraction intensity of the film located at the specific reciprocal coordinate. As shown in Figure 2d, the biaxial compressive distortion of the film material is demonstrated by the negative $\varepsilon_{\parallel,\text{Avr.}}$, and the positive $\varepsilon_{\perp,\text{Avr.}}$ from the respective cross-plane transverse expansion. With an increased film thickness of $\text{SrNb}_{0.2}\text{Ti}_{0.8}\text{O}_3/\text{SrTiO}_3(001)$ and the resultant strain relaxation,

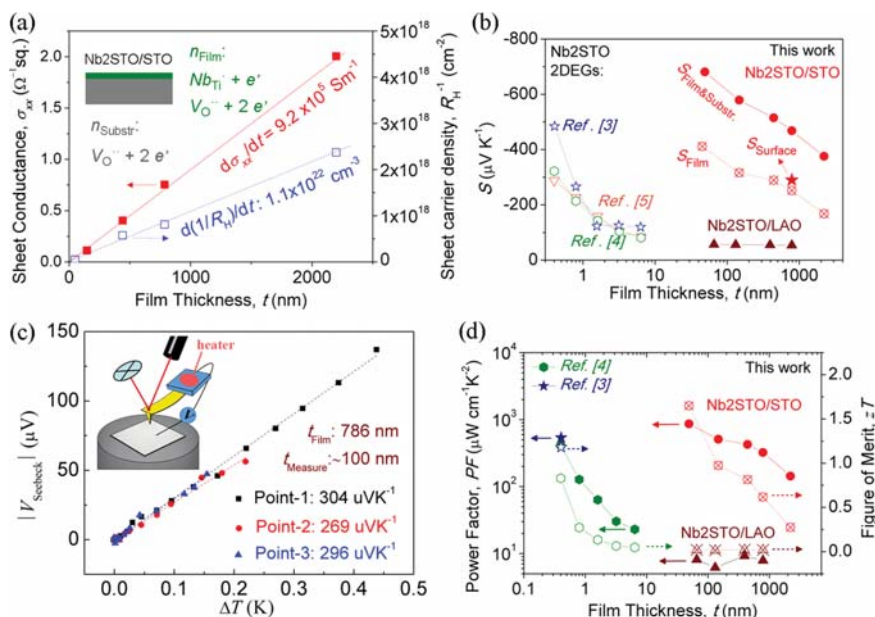


Figure 3. (a) Sheet conductance (σ_{xx}) and sheet carrier density (the reciprocal of Hall resistance, R_H^{-1}) as a function of film thickness (t) at room temperature for $\text{SrNb}_{0.2}\text{Ti}_{0.8}\text{O}_3/\text{SrTiO}_3(001)$. (b) Directly measured Seebeck coefficients for the film and substrate ($S_{\text{Film\&Substr}}$), the derived one (details given in Figure S7) for film materials (S_{Film}), and the localized S measured within 100 nm depth from the near-surface region of the film (S_{Surface}) using a nanometer-scale heating source in atomic force microscopy (AFM). (c) Seebeck voltage (V_{Seebeck}) vs temperature difference (ΔT) at the near-surface region of the film during the localized characterizations of S . More details are provided in Figure S6. (d) The estimated PF and zT . The S , PF, and zT reported for 2DEG- $\text{SrNb}_{0.2}\text{Ti}_{0.8}\text{O}_3$ ^{3–5} are plotted to be compared.

both $\varepsilon_{\parallel,\text{Avr}}$ and $\varepsilon_{\perp,\text{Avr}}$ tend toward to be zero. The effective lattice distortion is absent for $\text{SrNb}_{0.2}\text{Ti}_{0.8}\text{O}_3/\text{LaAlO}_3(001)$ owing to the complete relaxation of the interfacial strain. The distribution of in-plane lattice distortion was also derived from RSM by eq 2:

$$\begin{aligned} f(\varepsilon_{\parallel}) &= f\left(\frac{(1/Q_{\parallel}) - (1/Q_{\parallel 0})}{1/Q_{\parallel 0}}\right) \\ &= \frac{\int_{Q_{\perp}} I_{\text{Film}}(Q_{\parallel}, Q_{\perp}) dQ_{\perp(\parallel)}}{\iint_{Q_{\parallel} Q_{\perp}} I_{\text{Film}}(Q_{\parallel}, Q_{\perp}) dQ_{\parallel} dQ_{\perp}} \end{aligned} \quad (2)$$

The percentages of material distributed at each magnitude of in-plane lattice distortions $f(\varepsilon_{\parallel})$ for $\text{SrNb}_{0.2}\text{Ti}_{0.8}\text{O}_3/\text{SrTiO}_3(001)$ with different deposition thicknesses are shown in Figure 2e. A more broadened material distribution is clearly observed with an increased deposition thickness.

Figure 3 shows the TE performance for $\text{SrNb}_{0.2}\text{Ti}_{0.8}\text{O}_3/\text{SrTiO}_3(001)$ and $\text{SrNb}_{0.2}\text{Ti}_{0.8}\text{O}_3/\text{LaAlO}_3(001)$ grown under a comparable condition with varied thicknesses (t_{film}). Linear enhancements are observed for both sheet conductance (σ_{xx}) and sheet carrier density (R_H^{-1}) with increased t_{film} , as shown in Figure 3a. It indicates a constant conductivity, $\sigma = d(\sigma_{xx})/dt_{\text{film}}$, and carrier concentration, $n = d(R_H^{-1})/dt_{\text{film}}$, associated with the film deposition. Barely annealing the SrTiO_3 and LaAlO_3 substrates at the deposition atmosphere and temperature (650 °C) for 2 h without film depositions does not result in any detectable conductance. A large n of $\sim 1.1 \times 10^{22} \text{ cm}^{-3}$ associated with deposition is observed for $\text{SrNb}_{0.2}\text{Ti}_{0.8}\text{O}_3/\text{SrTiO}_3(001)$. This number is much larger compared to the ones grown on a $\text{LaAlO}_3(001)$ substrate under the same conditions ($\sim 6 \times 10^{21} \text{ cm}^{-3}$, with the carrier contributed by both the Nb dopant and oxygen vacancy) or the reported

values at a similar doping content.^{26–30} Similar effects were attributed to both intrinsic and extrinsic reasons, as summarized in previous literature reports.^{7–9,21,31,32} The intrinsic one includes distortion or polaron-induced $\text{Ti}-t_{2g}$ orbital reconfiguration²¹ and formation of 2DEGs by interfacial polarization,^{7–9} while the extrinsic one is the deposition-associated generation of V_O^{--} and free electron carriers within the SrTiO_3 substrate.^{31,32}

Figure 3b shows the directly measured Seebeck coefficient of the $\text{SrNb}_{0.2}\text{Ti}_{0.8}\text{O}_3/\text{SrTiO}_3(001)$ and $\text{SrNb}_{0.2}\text{Ti}_{0.8}\text{O}_3/\text{LaAlO}_3(001)$ samples ($S_{\text{Film\&Substr}}$), compared with the previously reported 2DEGs.^{3–5} As-measured $S_{\text{Film\&Substr}}$ is the averaged Seebeck coefficient of the film (S_{Film}) and substrate (S_{Substr}) weighted by their proportion in contributed electrical conductance. By attributing the net increase in n of $\text{SrNb}_{0.2}\text{Ti}_{0.8}\text{O}_3/\text{SrTiO}_3(001)$ compared to that of $\text{SrNb}_{0.2}\text{Ti}_{0.8}\text{O}_3/\text{LaAlO}_3(001)$ completely to the extrinsic conductance of the SrTiO_3 substrate, the Seebeck coefficient of the thin film (S_{Film}) was calculated. This prohibits the overestimation of S_{Film} , and more details on derivations are provided in the Supporting Information (SI), section C. It is worth noting that if there is any intrinsic enhancement in n or the depth distribution of V_O^{--} is smaller than the thickness of the substrate, the practical S_{Film} will be larger than the calculated ones shown in Figure 3b, as detailed in more discussions given in Figure S3b,c. Despite the potential underestimation, significant enhancements in S_{Film} are found in $\text{SrNb}_{0.2}\text{Ti}_{0.8}\text{O}_3/\text{SrTiO}_3(001)$ compared with $\text{SrNb}_{0.2}\text{Ti}_{0.8}\text{O}_3/\text{LaAlO}_3(001)$ and the reported bulk $\text{SrNb}_{0.2}\text{Ti}_{0.8}\text{O}_3$.²⁶ Increasing t_{film} from 45 nm to 2.2 μm reduces S_{Film} by $\sim 200 \mu\text{V K}^{-1}$, while the 2.2 μm thick film maintains S_{Film} approaching to be $\sim 170 \mu\text{V K}^{-1}$. This is in contrast to a much sharper decrease in S by $\sim 400 \mu\text{V K}^{-1}$ reported in $\text{SrNb}_{0.2}\text{Ti}_{0.8}\text{O}_3$ 2DEGs^{3–5} when the t_{film} was only increased from one to three unit cells (S_{Film} similar to the bulk

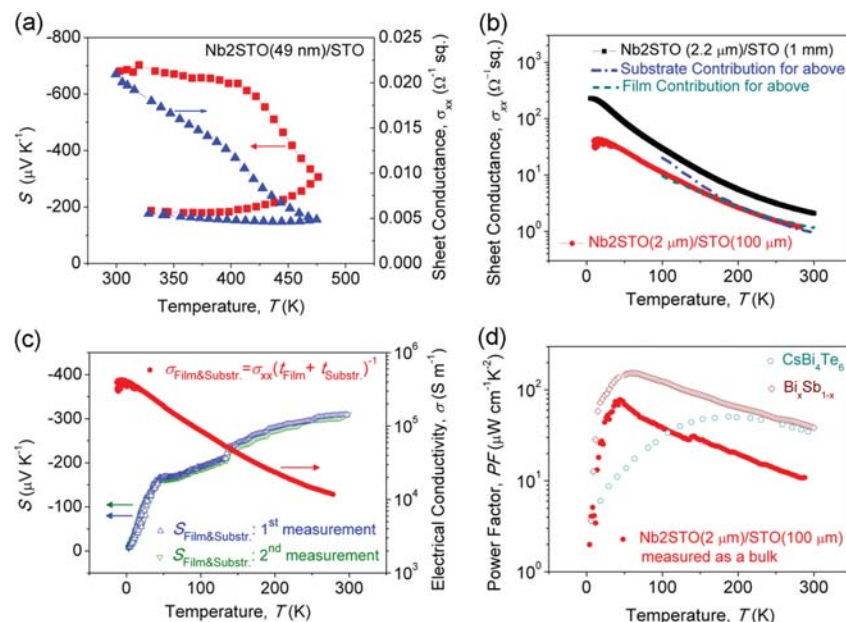


Figure 4. (a) Seebeck coefficient and sheet conductance of a 49 nm thick $\text{SrNb}_{0.2}\text{Ti}_{0.8}\text{O}_3/\text{SrTiO}_3(001)$ measured with a raising temperature up to 200 °C followed by a cooling down technique with a constant speed of $0.3\text{ }^\circ\text{C min}^{-1}$ in vacuum. (b) Sheet conductance of a $2.2\text{ }\mu\text{m}$ thick $\text{SrNb}_{0.2}\text{Ti}_{0.8}\text{O}_3$ film grown on a 1 mm thick $\text{SrTiO}_3(001)$ substrate and a $2\text{ }\mu\text{m}$ thick $\text{SrNb}_{0.2}\text{Ti}_{0.8}\text{O}_3$ film grown on a $100\text{ }\mu\text{m}$ thick $\text{SrTiO}_3(001)$ substrate as a function of temperature. The contributions from both the film and substrate to the sheet conductance are separated for the $\text{SrNb}_{0.2}\text{Ti}_{0.8}\text{O}_3$ ($2.2\text{ }\mu\text{m}$)/ SrTiO_3 (1 mm) sample (details are provided in the SI, section D). (c) Seebeck coefficients and electrical conductivities and (d) PFs of the $\text{SrNb}_{0.2}\text{Ti}_{0.8}\text{O}_3$ ($2\text{ }\mu\text{m}$)/ SrTiO_3 ($100\text{ }\mu\text{m}$) sample measured as bulk material (accounting for the thicknesses of the film and substrate), compared with conventional TE materials for low-temperature applications, such as $\text{Bi}_x\text{Sb}_{1-x}$ ¹⁵ and CsBi_4Te_6 .¹⁶

value at $t_{\text{Film}} \approx 1.2\text{ nm}$). Further consistency was achieved from the localized S near-surface regions with response a depth of $\sim 100\text{ nm}$ for a 800 nm thick film measured by using a nanometer-scale heating source in atomic force microscopy ($S_{\text{Near-Surf.}} = 290 \pm 18\text{ }\mu\text{V K}^{-1}$, as shown by Figure 3c). More details for the localized characterizations of S are given by Figure S7.

The PFs calculated for the films are from 10^2 to $10^3\text{ }\mu\text{W cm}^{-1}\text{ K}^{-2}$ when the deposition thickness reduces from $2.2\text{ }\mu\text{m}$ to 49 nm (see Figure 3d). Because there is no effective way yet to accurately measure the thermal conductivity, the κ values were estimated according to ref 3 ($\kappa = \kappa_{\text{Lattice}} + \kappa_{\text{Carrier}}$, where $\kappa_{\text{Lattice}} \approx 12\text{ W m}^{-1}\text{ k}^{-1}$, $\kappa_{\text{Carrier}} = L_0\sigma T$, and $L_0 = 2.45 \times 10^{-8}\text{ W }\Omega^{-1}\text{ K}^{-2}$). The resultant zT values are estimated to be from 0.3 to 1.6 with a reducing deposition thickness from $2.2\text{ }\mu\text{m}$ to 49 nm (see Figure 3d). The achieved TE performance exceeds the one measured for a film grown on a LAO substrate at comparable conditions (see Figure S6) and a $\text{SrNb}_{0.2}\text{Ti}_{0.8}\text{O}_3$ bulk material by 2 orders of magnitude. This has been verified by extensive experimental studies (more detailed results are provided in the SI, section D). Apart from $\text{SrNb}_{0.2}\text{Ti}_{0.8}\text{O}_3$, similar enhancement has been also achieved in other material compositions, such as $\text{SrNb}_{0.4}\text{Ti}_{0.6}\text{O}_3$ (SI, see Figure S8). Vice versa, performing thermoshock or annealing in a vacuum to eliminate the interfacial coherency, relax the interfacial strain, or disturb the alignment of lattice polarons significantly reduces both S and σ , as shown in Figures 4a and S8.

To further saturate the generation of $\text{V}_0^{\bullet\bullet}$ within the substrate and reduce its influence on the directly measured TE performance, a $2\text{ }\mu\text{m}$ thick $\text{SrNb}_{0.2}\text{Ti}_{0.8}\text{O}_3$ film was grown on a $100\text{ }\mu\text{m}$ thick $\text{SrTiO}_3(001)$ substrate under the same conditions. As shown in Figure 4b, the σ_{xx} measured for $\text{SrNb}_{0.2}\text{Ti}_{0.8}\text{O}_3$ ($t_{\text{Film}} = 2\text{ }\mu\text{m}$)/ SrTiO_3 ($t_{\text{Substr.}} = 100\text{ }\mu\text{m}$)

overlaps with the derived film contribution ($\sigma_{xx,\text{Film}}$; its derivation is explained in the SI, section C) of $\text{SrNb}_{0.2}\text{Ti}_{0.8}\text{O}_3$ ($t_{\text{Film}} = 2.2\text{ }\mu\text{m}$)/ SrTiO_3 ($t_{\text{Substr.}} = 1\text{ mm}$) at $100\text{--}300\text{ K}$. It reveals a significantly reduced proportion of σ_{xx} from the substrate associated with the saturation of the $\text{V}_0^{\bullet\bullet}$ concentration at the reduced amount of substrate material. This provides further opportunities to more directly characterize the TE properties associated with the film material. Figure 4c shows the temperature-dependent S and electrical conductivity, $\sigma = \sigma_{xx}(t_{\text{Film}} + t_{\text{Substr.}})$, of the $\text{SrNb}_{0.2}\text{Ti}_{0.8}\text{O}_3$ ($2\text{ }\mu\text{m}$)/ SrTiO_3 ($100\text{ }\mu\text{m}$) sample measured in bulk by accounting for the thickness of the substrate. Similar to the reported $\text{SrNb}_x\text{Ti}_{1-x}\text{O}_3$ single-crystalline materials,^{27,29,30} elevating the temperature enhances S and decreases σ . The two discontinuous steps observed in the S -T curve at ~ 40 and 150 K are confirmed to be intrinsic associated to the present sample, which may be associated with the phonon drags contributed by the film and substrate at different carrier concentrations reported previously by ref 3. Even taking the thickness of the substrate into account, a bulk PF (integrating the thicknesses of both the film and substrate) of $78\text{ }\mu\text{W cm}^{-1}\text{ K}^{-2}$ is achievable at low temperatures, as shown in Figure 4d.

In contrast to the previous 2DEG-related $\text{SrNb}_{0.2}\text{Ti}_{0.8}\text{O}_3$ ³⁻⁵ the enhanced Seebeck coefficient for $\text{SrNb}_{0.2}\text{Ti}_{0.8}\text{O}_3/\text{SrTiO}_3(001)$ in this work is not strongly related to spatial confinements. The present achieved performance is comparable with the one for oxygen-annealed $\text{LaAlO}_3/\text{SrTiO}_3$, in which case similar magnitudes of S ($\sim 600\text{ }\mu\text{V K}^{-1}$) at large n_{2D} (an order of high 10^{13} up to 10^{14} cm^{-2}) were achieved by interfacial polarization-induced EPC.^{7,8} The high relative permittivity ($\epsilon_r \sim 10^3$) and ferroelectric nature of strain-distorted SrTiO_3 ²³ make an electronic 2D confinement of carriers by the aligned

domains of lattice polarons be practicable (see more detailed discussions in the SI, Figure S9).

Following this understanding, an increasing deposition thickness weakens the strain-induced lattice polarization and/or reduces their ordering in alignment, as previously demonstrated in Figure 2d,e, respectively. As a result, the 2D confinements of carriers by lattice polarization are expected to be reduced. This is in agreement with the reducing trend in the Seebeck coefficient with an increasing film thickness.

The relevance to lattice/interfacial polarization is also demonstrated by the anisotropy observed in the Seebeck coefficient when growing $\text{SrNb}_{0.2}\text{Ti}_{0.8}\text{O}_3$ on a SrTiO_3 substrate with other orientations from tilting the direction of lattice polarization. For example, as compared to $\text{SrNb}_{0.2}\text{Ti}_{0.8}\text{O}_3/\text{SrTiO}_3(001)$ with the same thickness, $\text{SrNb}_{0.2}\text{Ti}_{0.8}\text{O}_3/\text{SrTiO}_3(110)$ exhibits similar electrical conductance and interfacial strains but shows a significantly reduced Seebeck coefficient (see detailed results in Figure S10a). This observation is consistent with the previous reports that the [001] direction exhibits optimal ferroelectric behaviors for perovskite oxides with charge-center asymmetry.^{33,34} Following our previous understanding, a more effective well-like confinement of the carrier is expected for $\text{SrNb}_{0.2}\text{Ti}_{0.8}\text{O}_3/\text{SrTiO}_3(001)$ because the alignment of [001] lattice polarization is parallel to the interfacial polarization and perpendicular to the transportation plane of the carriers. In contrast, the 2D confinement of carriers is indirect for $\text{SrNb}_{0.2}\text{Ti}_{0.8}\text{O}_3/\text{SrTiO}_3$ because the [001] lattice polarization is offset by $\sim 45^\circ$ with respect to both the interfacial polarization and also to the electron transportation plane. Apart from the lattice polarization and its alignment, we also emphasize the relevance of the ultrahigh TE performance to the interfacial polarization, which is assumed to be coupled with the strain-induced lattice polarizations. This is further demonstrated for compressive-strained $\text{SrNb}_{0.2}\text{Ti}_{0.8}\text{O}_3$ grown on $\text{DyScO}_3(001)$ substrates, which shows similar TE performance to that of the bulk material (see Figure S10).

In summary, ultrahigh TE performance of the 2DEG-related material has been achieved in $\text{SrNb}_{0.2}\text{Ti}_{0.8}\text{O}_3$ oxide films at a submicrometer-scale thickness by regulating strain-induced lattice polarizations and interfacial polarizations. As compared to the reported 2DEG $\text{SrNb}_{0.2}\text{Ti}_{0.8}\text{O}_3$, the critical film thickness to preserve a large Seebeck coefficient at a high carrier concentration is significantly improved from the previous subnanometer scale to a submicrometer scale. A large zT up to 1.6 and ultrahigh PF of $\sim 10^3 \mu\text{W cm}^{-1} \text{K}^{-2}$ were achieved at room temperature. These performances exceed those of all existing n-type TE materials and the best TE oxide materials beyond a subnanometer scale for room-temperature use. The strain-induced lattice polarization and its relative alignment with the interfacial polarization are demonstrated to strongly affect the TE properties. These observations shed light on the possible mechanisms that are relevant to polarization- and polar discontinuity-induced 2D carrier confinements. Beyond the ultrahigh TE performance, the present oxide films are less toxic and not largely dependent on heavy elements, such as Bi, Sb, or Te. This favors potential applications in microscale energy harvesters, on-chip coolings, and thermal sensors used at room temperature or below.

■ ASSOCIATED CONTENT

S Supporting Information

The Supporting Information is available free of charge on the ACS Publications website at DOI: 10.1021/acsenergylett.7b00197.

Experimental details, additional structural results from XRD and RSM, detailed derivations to separate the contribution of the film and substrate to the TE performance, more results to confirm the observed high TE performance in this work, additional calculated and experimental results to demonstrate the relevance of the present high TE performance to alignment of lattice polarizations, and the contributions of each author (PDF)

■ AUTHOR INFORMATION

Corresponding Authors

*E-mail: cld@mail.sic.ac.cn (L.C.).

*E-mail: jikunchen@ustb.edu.cn (J.C.). Also the contact for materials' requests.

ORCID

Jikun Chen: 0000-0002-0351-6657

Nuofu Chen: 0000-0002-9584-0699

Present Address

^oJ.C.: School of Engineering, The University of Tokyo, Tokyo 1138656, Japan.

Author Contributions

^oJ.C. and H.C. contributed equally to this work. J.C. proposed the idea, planned for the experiments, developed the film deposition strategy, performed film growth, and wrote the manuscript, assisted by L.C.; H.C. and F.H. performed the verification experiments, advised by L.C., J.C., X.S., and H.Z.; H.C., F.H., K.Z., and T.Z. characterized the transportation performances; J.C., X.K., and W.W. contributed to the RSM measurement and analysis; B.G., F.H., and H.D. contributed to the TEM measurement; M.D. performed the RBS measurement; and Y.T., N.C., and Y.J. provided experimental support and useful discussions.

Notes

The authors declare no competing financial interest.

■ ACKNOWLEDGMENTS

This work is supported by the Fundamental Research Funds for the Central Universities (USTB), National Natural Science Foundation of China (No. 51602022, No. 61674013, and No. 11374332), the key research program of Chinese Academy of Sciences (Grant No. KGZD-EW-T06), a research grant from the Shanghai government (No. 15JC1400301), and the National Key R&D Program of China (2016YFA0201103). J.C. also appreciates the Japanese Society for the Promotion of Science (Fellowship ID: P15363). We appreciate helpful discussions with or technical support by Prof. Akira Toriumi from The University of Tokyo (Japan), Prof. Jian Shi from Rensselaer Polytechnic Institute (U.S.A.), Prof. Rafael Jaramillo from Massachusetts Institute of Technology (U.S.A.), Prof. Xuchun Gui from Sun Yat-sen University (China), Prof. Renkui Zheng from Shanghai Institute of Ceramics, Chinese Academy of Sciences (China), and Mr. Kiyoshi Ogawa from Ozawa Science Co. Ltd. Japan. Mr. Charles Plumridge from The University of Tokyo is acknowledged for revising this manuscript.

■ REFERENCES

- (1) Venkatasubramanian, R.; Siivola, E.; Colpitts, T.; O'Quinn, B. Thin-film thermoelectric devices with high room-temperature figures of merit. *Nature* **2001**, *413*, 597–602.
- (2) Harman, T. C.; Taylor, P. J.; Walsh, M. P.; LaForge, B. E. Quantum dot superlattice thermoelectric materials and devices. *Science* **2002**, *297*, 2229–2232.
- (3) Ohta, H.; Kim, S.; Mune, Y.; Mizoguchi, T.; Nomura, K.; Ohta, S.; Nomura, T.; Nakanishi, Y.; Ikuhara, Y.; Hirano, M.; et al. Giant thermoelectric Seebeck coefficient of a two-dimensional electron gas in SrTiO_3 . *Nat. Mater.* **2007**, *6*, 129–134.
- (4) Mune, Y.; Ohta, H.; Koumoto, K.; Mizoguchi, T.; Ikuhara, Y. Enhanced Seebeck coefficient of quantum-confined electrons in $\text{SrTiO}_3/\text{SrTi}_{0.8}\text{Nb}_{0.2}\text{O}_3$ superlattices. *Appl. Phys. Lett.* **2007**, *91*, 192105.
- (5) Lee, K. H.; Mune, Y.; Ohta, H.; Koumoto, K. Thermal Stability of Giant Thermoelectric Seebeck Coefficient for $\text{SrTiO}_3/\text{SrTi}_{0.8}\text{Nb}_{0.2}\text{O}_3$ Superlattices at 900K. *Appl. Phys. Express* **2008**, *1*, 015007.
- (6) Dresselhaus, M. S.; Chen, G.; Tang, M. Y.; Yang, R. G.; Lee, H.; Wang, D. Z.; Ren, Z. F.; Fleuriol, Z. P.; Gogna, P.; Fleuriol, Z. P.; et al. New directions for low-dimensional thermoelectric materials. *Adv. Mater.* **2007**, *19*, 1043–1053.
- (7) Pallecchi, I.; Telesio, F.; Marré, D.; Li, D.; Gariglio, S.; Triscone, J. M.; Filippetti, A. Large phonon-drag enhancement induced by narrow quantum confinement at the $\text{LaAlO}_3/\text{SrTiO}_3$ interface. *Phys. Rev. B: Condens. Matter Mater. Phys.* **2016**, *93*, 195309.
- (8) Pallecchi, I.; Telesio, F.; Li, D. F.; Fête, A.; Gariglio, S.; Triscone, J. M.; Filippetti, A.; Delugas, P.; Fiorentini, V.; Marré, D. Giant oscillating thermopower at oxide interfaces. *Nat. Commun.* **2015**, *6*, 6678.
- (9) Renshaw Wang, X.; Sun, L.; Huang, Z.; Lü, W. M.; Motapothula, M.; Annadi, A.; Liu, Z. Q.; Zeng, S. W.; Venkatesan, T.; Ariando. Parallel charge sheets of electron liquid and gas in $\text{La}_{0.5}\text{Sr}_{0.5}\text{TiO}_3/\text{SrTiO}_3$ heterostructures. *Sci. Rep.* **2016**, *5*, 18282.
- (10) Zheng, L.; Li, W.; Lin, S.; Li, J.; Chen, Z.; Pei, Y. Interstitial defects improving thermoelectric SnTe in addition to band convergence. *ACS Energy Lett.* **2017**, *2*, 563–568.
- (11) Roychowdhury, S.; Panigrahi, R.; Perumal, S.; Biswas, K. Ultrahigh Thermoelectric Figure of Merit and Enhanced Mechanical Stability of p-type $\text{AgSb}_{1-x}\text{Zn}_x\text{Te}_2$. *ACS Energy Lett.* **2017**, *2*, 349–356.
- (12) Tan, G.; Zhao, L. D.; Kanatzidis, M. G. Rationally designing high-performance bulk thermoelectric materials. *Chem. Rev.* **2016**, *116*, 12123–12149.
- (13) Pei, Y. Z.; Shi, X. Y.; LaLonde, A.; Wang, H.; Chen, L. D.; Snyder, G. J. Convergence of electronic bands for high performance bulk thermoelectrics. *Nature* **2011**, *473*, 66–69.
- (14) Hu, L.; Wu, H.; Zhu, T.; Fu, C.; He, J.; Ying, P.; Zhao, X. Tuning multiscale microstructures to enhance thermoelectric performance of n-Type bismuth telluride based solid solutions. *Adv. Energy Mater.* **2015**, *5*, 1500411.
- (15) Lenoir, B.; Dauscher, A.; Cassart, M.; Ravich, Y. I.; Scherrer, H. Effect of antimony content on the thermoelectric figure of merit of $\text{Bi}_{1-x}\text{Sb}_x$ alloys. *J. Phys. Chem. Solids* **1998**, *59*, 129–134.
- (16) Chung, D. Y.; Hogan, T.; Brazis, P.; Roccia-Lane, M.; Kannewurf, C.; Bastea, M.; Uher, C.; Kanatzidis, M. G. CsBi_4Te_6 : A high-performance thermoelectric material for low-temperature applications. *Science* **2000**, *287*, 1024–1027.
- (17) Ambacher, O.; Smart, J.; Shealy, J. R.; Weimann, N. G.; Chu, K.; Murphy, M.; Schaff, W. J.; Eastman, L. F.; Dimitrov, R.; Wittmer, L.; et al. Two-dimensional electron gases induced by spontaneous and piezoelectric polarization charges in N- and Ga-face AlGaN/GaN heterostructures. *J. Appl. Phys.* **1999**, *85*, 3222–3233.
- (18) Ibbetson, J. P.; Fini, P. T.; Ness, K. D.; Denbaars, S. P.; Speck, J. S.; Mishra, U. K. Polarization effects, surface states, and the source of electrons in AlGaN/GaN heterostructure field effect transistors. *Appl. Phys. Lett.* **2000**, *77*, 250–252.
- (19) Tsukazaki, A.; Ohtomo, A.; Kita, T.; Ohno, Y.; Ohno, H.; Kawasaki, M. Quantum Hall effect in polar oxide heterostructures. *Science* **2007**, *315*, 1388–1391.
- (20) Stemmer, S.; Allen, S. J. Two-dimensional electron gases at complex oxide interfaces. *Annu. Rev. Mater. Res.* **2014**, *44*, 151–171.
- (21) Ohtomo, A.; Muller, D. A.; Grazul, J. L.; Hwang, H. Y. Artificial charge-modulation in atomic-scale perovskite titanate superlattices. *Nature* **2002**, *419*, 378–380.
- (22) Verma, A.; Raghavan, S.; Stemmer, S.; Jena, D. Ferroelectric transition in compressively strained SrTiO_3 thin films. *Appl. Phys. Lett.* **2015**, *107*, 192908.
- (23) Haeni, J. H.; et al. Room-temperature ferroelectricity in strained SrTiO_3 . *Nature* **2004**, *430*, 758–761.
- (24) Uwe, H.; Sakudo, T.; et al. Stress-induced ferroelectricity and soft phonon modes in SrTiO_3 . *Phys. Rev. B* **1976**, *13*, 271–286.
- (25) Pertsev, N. A.; Tagantsev, A. K.; Setter, N. Phase transitions and strain-induced ferroelectricity in SrTiO_3 epitaxial thin films. *Phys. Rev. B: Condens. Matter Mater. Phys.* **2000**, *61*, R825.
- (26) Wang, Y.; Lee, K. H.; Ohta, H.; Koumoto, K. Thermoelectric properties of electron doped $\text{SrO}(\text{SrTiO}_3)_n$ ($n = 1, 2$) ceramics. *J. Appl. Phys.* **2009**, *105*, 103701–103706.
- (27) Ohta, H.; Sugiura, K.; Koumoto, K. Recent progress in oxide thermoelectric materials: p-type $\text{Ca}_3\text{Co}_4\text{O}_9$ and n-type SrTiO_3 . *Inorg. Chem.* **2008**, *47*, 8429–8436.
- (28) Okuda, T.; Nakanishi, K.; Miyasaka, S.; Tokura, Y. Large thermoelectric response of metallic perovskites: $\text{Sr}_{1-x}\text{La}_x\text{TiO}_3$ ($0 \leq x \leq 0.1$). *Phys. Rev. B: Condens. Matter Mater. Phys.* **2001**, *63*, 113104.
- (29) Frederikse, H. P. R.; Thurber, W. R.; Hosler, W. R. Electronic Transport in strontium titanate. *Phys. Rev.* **1964**, *134*, A442.
- (30) Cain, T. A.; Kajdos, A. P.; Stemmer, S. La-doped SrTiO_3 films with large cryogenic thermoelectric power factors. *Appl. Phys. Lett.* **2013**, *102*, 182101.
- (31) Chen, J.; Döbeli, M.; Stender, D.; Lee, M. M.; Conder, K.; Schneider, C. W.; Wokaun, A.; Lippert, T. Tracing the origin of oxygen for $\text{La}_{0.6}\text{Sr}_{0.4}\text{MnO}_3$ thin film growth by pulsed laser deposition. *J. Phys. D: Appl. Phys.* **2016**, *49*, 045201.
- (32) Schneider, C. W.; Esposito, M.; Marozau, I.; Conder, K.; Doebeli, M.; Hu, Y.; Mallepell, M.; Wokaun, A.; Lippert, T. The origin of oxygen in oxide thin films: Role of the substrate. *Appl. Phys. Lett.* **2010**, *97*, 192107.
- (33) Luo, B. C.; Wang, D. Y.; Duan, M. M.; Li, S. Orientation-dependent piezoelectric properties in lead-free epitaxial $0.5\text{BaZr}_{0.2}\text{Ti}_{0.8}\text{O}_3$ - $0.5\text{Ba}_{0.7}\text{Ca}_{0.3}\text{TiO}_3$ thin films. *Appl. Phys. Lett.* **2013**, *103*, 122903.
- (34) Xu, R.; Liu, S.; Grinberg, I.; Karthik, J.; Damodaran, A. R.; Rappe, A. M.; Martin, L. W. Ferroelectric polarization reversal via successive ferroelastic transitions. *Nat. Mater.* **2014**, *14*, 79–86.